Comprehensive Characterization and Optoelectronic Significance of Ho^{3+} and Cr^{3+} Co-doped $ZnAl_2O_4$ Spinels

I. Elhamdi,*[,1] H. Souissi,[1] S. Kammoun,[1] E. Dhahri,[1]J. Pina,[2] B. F. O. Costa[3], E. López- Lago[4]

[1]*Laboratoire de Physique Appliquée, Faculté des Sciences, Université de Sfax, Tunisie.*
[2]*University of Coimbra, CQC-IMS, Department of Chemistry, 3004-535 Coimbra, Portugal.*
[3]*University of Coimbra, CFisUC, Physics Department, 3004-516 Coimbra, Portugal.*
[4]*Departamento de Física Aplicada, Facultade de Óptica e Optometría, Campus Vida, Universidade de Santiago de Compostela (USC), 15782 Galicia, Spain.*

*** Corresponding Author**: imen.elhamdi.etud@fss.usf.tn

ABSTRACT

The spinels $ZnAl_{1.99-x}Ho_xCr_{0.01}O_4$ (with x=0, 0.001) were synthesized using a solid-state method, and various techniques were employed for their characterization. X-ray diffraction (XRD) analysis confirmed a cubic spinel structure with the $Fd\bar{3}m$ space group for both spinels. The morphology and homogeneity of the chemical composition were identified through Scanning Electron Microscopy (SEM) and Energy Dispersive X-ray analysis. Raman and infrared vibrational spectroscopy techniques were also employed for analysis. The optical band gap (Eg) was determined from UV/Vis absorption spectra, and the direct transition behavior was confirmed by Tauc's law. The observed large disorder and defects concentration are attributed to the presence of Cr^{3+} and Ho^{3+} ions, explain this behavior. The Electron Paramagnetic Resonance (EPR) measurement presented different types of traps. Room temperature absorption spectra exhibited multiple peaks corresponding to the 3d-3d and 4f-4f transitions of Cr^{3+} and Ho^{3+} ions. The results obtained validate the significance of our compounds in optoelectronic device applications.

Keywords: spinel oxide; Raman; FTIR; UV/Vis spectroscopy; Optical band-gap; EPR measurement.

1. Introduction

The spinel family, characterized by the general formula AB_2O_4, plays a pivotal role in the realm of oxide materials, showcasing exceptional physical properties that have garnered significant attention [1-11]. This intriguing composition involves a metal cation (A) occupying a tetrahedral (Td) site, typically represented by elements like Zn^{2+} or Mg^{2+}, while a cation (B) fills an octahedral (Oh) site, commonly represented by elements such as Al^{3+} or Ga^{3+}.

What distinguishes spinels even further is their versatility as luminous matrices. The B-site of spinels accommodates various luminescent activators, including ions of transition metals (TM) or lanthanides (Ln), resulting in a broad spectrum of spinels with captivating luminescent properties [5,6,11]. This unique characteristic opens up a myriad of possibilities in the field of optoelectronics, where the marriage of optical and structural properties makes spinels highly desirable.

In the realm of optoelectronics, spinels find applications in diverse areas. They serve as key components in optical windows and lenses, contributing to the development of high-quality optical systems. Additionally, spinels play a crucial role in the fabrication of optical waveguides, enabling the efficient transmission of light signals. The unique properties of spinels make them valuable components in optical sensors, offering enhanced sensitivity and precision.

Furthermore, spinels contribute to the field of optoelectronics through their application in antireflection coatings. Their ability to minimize reflection ensures improved light transmission and optical performance. Additionally, spinels find utility in the development of optoelectronic chips, where their structural and luminescent properties enhance the functionality and efficiency of these electronic devices.

Recently, studies have been done on the structural, electrical, vibrational, and optical characteristics of a novel spinel persistent phosphor of $ZnAl_{0.095}Cr_{0.05}O_4$ prepared by solid-state and sol-gel techniques [5,6,11].

The interpretation of the ambient temperature Raman and infrared (ATR-IR) spectra has been completed. The direct transition behavior has been confirmed using Tauc's law, and the optical band gap E_g has been determined from absorption UV/vis spectra. The value of the Urbach energy E_u is estimated to be 0.63 eV for $ZnAl_{1.95}Cr_{0.05}O_4$ indicating a disorder condition in this spinel. The electronic structure of Cr^{3+}, with $3d^3$ electronic configuration, was determined via a crystal field analysis in the O_h symmetry site using the absorption and photoluminescence excitation (PLE) spectra [5,6,11].

In this study, $ZnAl_{1.99-x}Ho_xCr_{0.01}O_4$ (with x=0, 0.001) spinels were synthesized through solid-state reaction and subsequently characterized using structural and optical techniques. The Ho^{3+} ion, belonging to the Lanthanide family with an electron configuration of $4f^{10}$, was incorporated into the spinel lattice. The X-ray Diffraction technique confirmed the cubic structure, with the space group identified as $Fd\bar{3}m$. Raman, FTIR, and UV-Vis absorption spectroscopy were employed for a detailed analysis of the optical properties. The optical band gap (E_g) was determined, shedding light on the nature and value of the band gap. Room temperature UV-Vis absorbance spectra of the $ZnAl_{1.99-x}Ho_xCr_{0.01}O_4$ (with x=0, 0.001) spinels were analyzed, revealing the 3d-3d transitions of Cr^{3+} and 4f-4f transitions of Ho^{3+}. The study primarily focuses on understanding the pertinent factors influencing the electronic behavior of the Cr^{3+} ion within the spinel lattice, particularly in light of the substitution of Ho^{3+} by Al^{3+} in the host material.

2. Experimental details

The $ZnAl_{1.99-x}Ho_xCr_{0.01}O_4$ (with x=0, 0.001) samples were prepared by the solid-state method from adequate mixtures of $ZnCO_3$ (98%), Ho_2O_3(99%), Cr_2O_3 (99%) and Al_2O_3 (99%) analytical reagents were purchased from Sigma-Aldrich and utilized directly after purchase without purification. The powders were first annealed at 700°C for 24 h, then ground using an agate mortar and pelletized. The latter undergo progressive heating up to 1200°C for sintering, each time for a duration of 24 hours.

The X-ray powder diffractometer (X-Ray Siemens D5000) was used to analyze the crystal structures using a $CuK\alpha_1$ radiation source (λ = 1.5406 Å). Data were acquired in the 2θ range of 20°–100° with a step size of 0.02°. The Raman spectra were obtained in the 20-1000 cm^{-1} range using a Horiba LabRam HR Evolution micro-Raman confocal system, with excitation at = 532 nm. A TESCAN VEGA3 SBH scanning electron microscope (SEM) fitted with an energy dispersive microscopy (EDS detector Bruker XFlagh 410 M) was used to analyze the powder's morphology to determine the homogeneity of the chemicals. An AvaSpec-ULS-TEC Avantes Senseline Fiber Optic Spectrometer System connected to a Mikropack DH-2000-BAL UV-Vis-NIR light source was used to measure reflectance to record solid-state absorption spectra. The FTIR study was recorded using Thermo Scientific Nicolet 6700 equipment, which operates in the 400–4000 cm^{-1} range. The room temperature EPR spectra of powder samples deposited in a 10 µL glass capillary (Duran Ringcaps, Hirschmann, Germany) were obtained using a MiniScope MS 400 X-band EPR spectrometer (Magenttech Germany) equipped with a Suprasil Nitrogen Dewar (SP Wilmad-LabGlass, USA). Software utilized was ImageJ and the

Visualization Electronic and STructural Analysis VESTA (Version 3 Copyright (C) 2006-2022, Koichi Momma and Fujio Izumi).

3. Results and discussion

3.1 X-ray Diffraction Study

X-ray diffraction XRD is a powerful technique used to determine the crystallographic phases, lattice parameters, and other structural characteristics. The XRD data is typically collected over a range of angles (2θ) to cover the entire diffraction pattern. This involves identifying the positions and intensities of the diffraction peaks. The experimental diffraction pattern can be compared to databases of known crystal structures to identify the phases present in the sample. Refinement techniques, such as Rietveld refinement, can be applied to improve the accuracy of the structural parameters obtained from the diffraction data. Figure 1 displays the X-ray diffraction patterns of $ZnAl_{1.99-x}Ho_xCr_{0.01}O_4$ (with x=0, 0.001) samples. The diffraction peaks are indexed to the reticular crystal planes of the cubic spinel structure phase $Fd\bar{3}m$ space group (220), (311), (400), (331), (422), (333), (511), (440), (620) and (533). This observation is made using the standard JCPDS data file. The X-ray diffractogram was refined using the Rietveld method, revealing the presence of two phases, with the spinel compound being the main phase and ZnO in low proportion as an impurity phase. There are numerous references to this impurity phase in the literature [5,6,12,13]. Table 1 displays the revised parameters of crystallography. The effective goodness of fit between the calculated and observed profiles is shown by the refinement quality factor χ2. Figure 2 shows the structure of the compounds $ZnAl_{1.99-x}Ho_xCr_{0.01}O_4$ (with x=0, 0.001). According to their figures, the Al^{3+} cation is found in octahedral coordination (O_h sites), while the Zn^{2+} cation is found in tetrahedral coordination (T_d sites). The octahedral location of Al^{3+} ions is replaced by the trivalent cations Ho^{3+} and Cr^{3+} (Figure 2) [14,15].

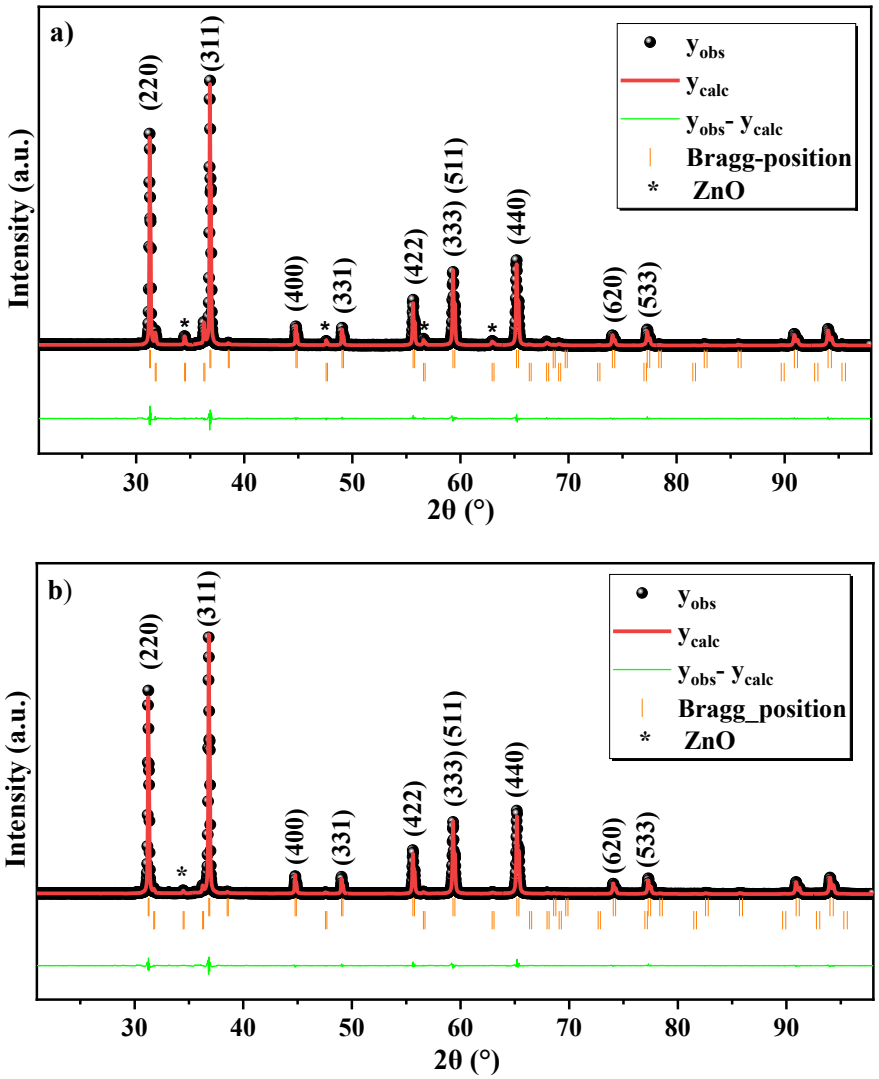

Figure 1. Rietveld refinement for $ZnAl_{1.99-x}Ho_xCr_{0.01}O_4$ spinels: a) x=0; b) x=0.001.

Table 1: Results of Rietveld refinements for $ZnAl_{1.99-x}Ho_xCr_{0.01}O_4$ (with x=0, 0.001)

Samples	$ZnAl_{1.99}Cr_{0.01}O_4$	$ZnAl_{1.989}Ho_{0.001}Cr_{0.01}O_4$
Space Group	$Fd\bar{3}m$	
a (Å)	8.089_2	8.089_5
v (Å^3)	529.318_1	529.377
Rp	7.86	7.52
Rwp	8.78	8.44
χ^2	3.987	3.714
Al-O (Å)	1.919_4	1.917_9
Al-O-Al (°)	96.321_4	96.43

ZnO (%)	4.76	1.50
D_{W-H} (nm)	66	68

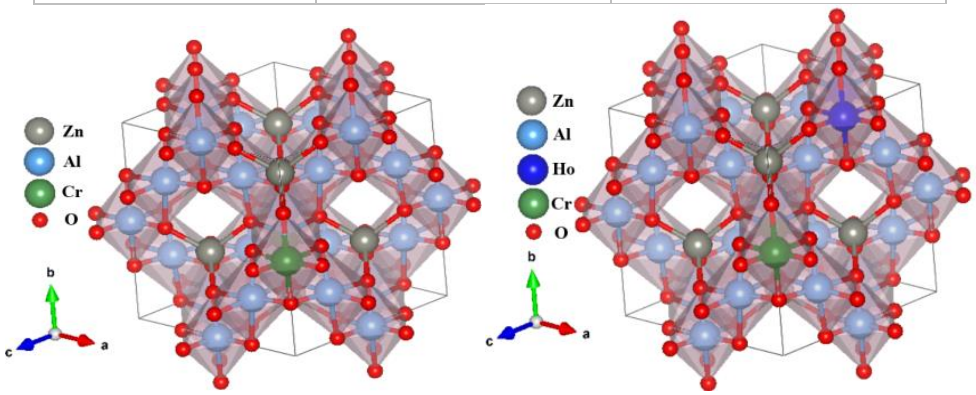

Figure 2. Structural illustration with Vesta software for $ZnAl_{1.99}Cr_{0.01}O_4$ and $ZnAl_{1.989}Ho_{0.001}Cr_{0.01}O_4$

The average crystallite size D_{W-H} was determined using the Williamson-Hall relation [16]:

$$\beta\cos(\theta) = \frac{K\lambda}{D_{W-H}} + 4\varepsilon\sin(\theta) \qquad (1)$$

where **ε** is the effective strain, λ (1.5406 Å) represents the used wavelength, θ is the Bragg angle, K is the shape factor and β is the full-width at half maximum (FWHM) of the diffraction peak. The intercept of the linear fit of βcos(θ) as a function of 4sin(θ) was used to obtain the value of the crystallite size (Figure 3). The obtained values are very similar (66 for 68 nm for the compound without and with Holmium, respectively) which means that the presence of Holmium has a negligible impact on particle size.

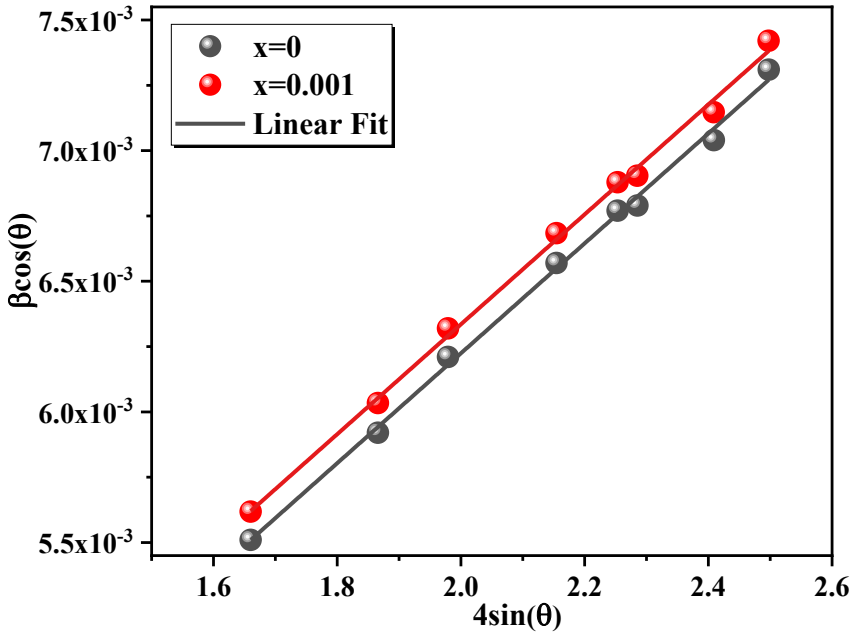

Figure 3. The Williamson-Hall plot of $ZnAl_{1.99-x}Ho_xCr_{0.01}O_4$ (with x=0, 0.001) compounds

3.2 SEM and EDX study

Scanning electron microscopy was used to examine the morphology of the particles contained in $ZnAl_{1.99-x}Ho_xCr_{0.01}O_4$ (with x=0, 0.001) compounds. The agglomerated and irregularly shaped grains are shown in Figure 4. These agglomerations are caused by the enormous surface area of the particles and their interaction with the weak Van der Waals force. The average particle size distribution was found to be centered at 304 nm for compound $ZnAl_{1.99}Cr_{0.01}O_4$ and 399 nm for compound $ZnAl_{1.989}Ho_{0.001}Cr_{0.01}O_4$ by Lorentz fitting using ImageJ software, as shown in Figure 4. To verify their chemical composition, we also showed the energy dispersion spectrum (EDS) of $ZnAl_{1.99-x}Ho_xCr_{0.01}O_4$ (with x=0, 0.001) samples in Figure 5. The presence of all the component chemical constituents of Ho^{3+}/ Cr^{3+} substituted $ZnAl_2O_4$, including Zn, Cr, Al, Ho, and O, is confirmed by the spectra, indicating the purity of our samples. On the other hand, from the map representations shown in Figure 5, we conclude the chemical elements that constitute this material are uniformly and homogeneously distributed. Table 2 displays the elements presented in the spinels $ZnAl_{1.99-x}Ho_xCr_{0.01}O_4$ (with x=0, 0.001) as well as their quantitative analysis.

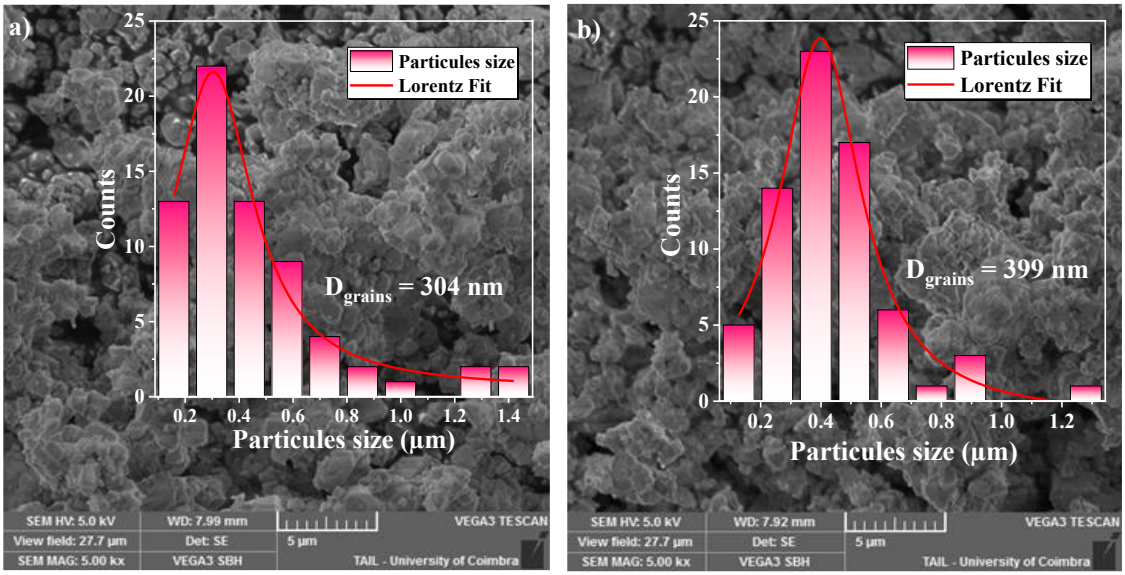

Figure 4. SEM image and the average particle size histograms of $ZnAl_{1.99-x}Ho_xCr_{0.01}O_4$ compounds: a) x=0; b) x=0.001.

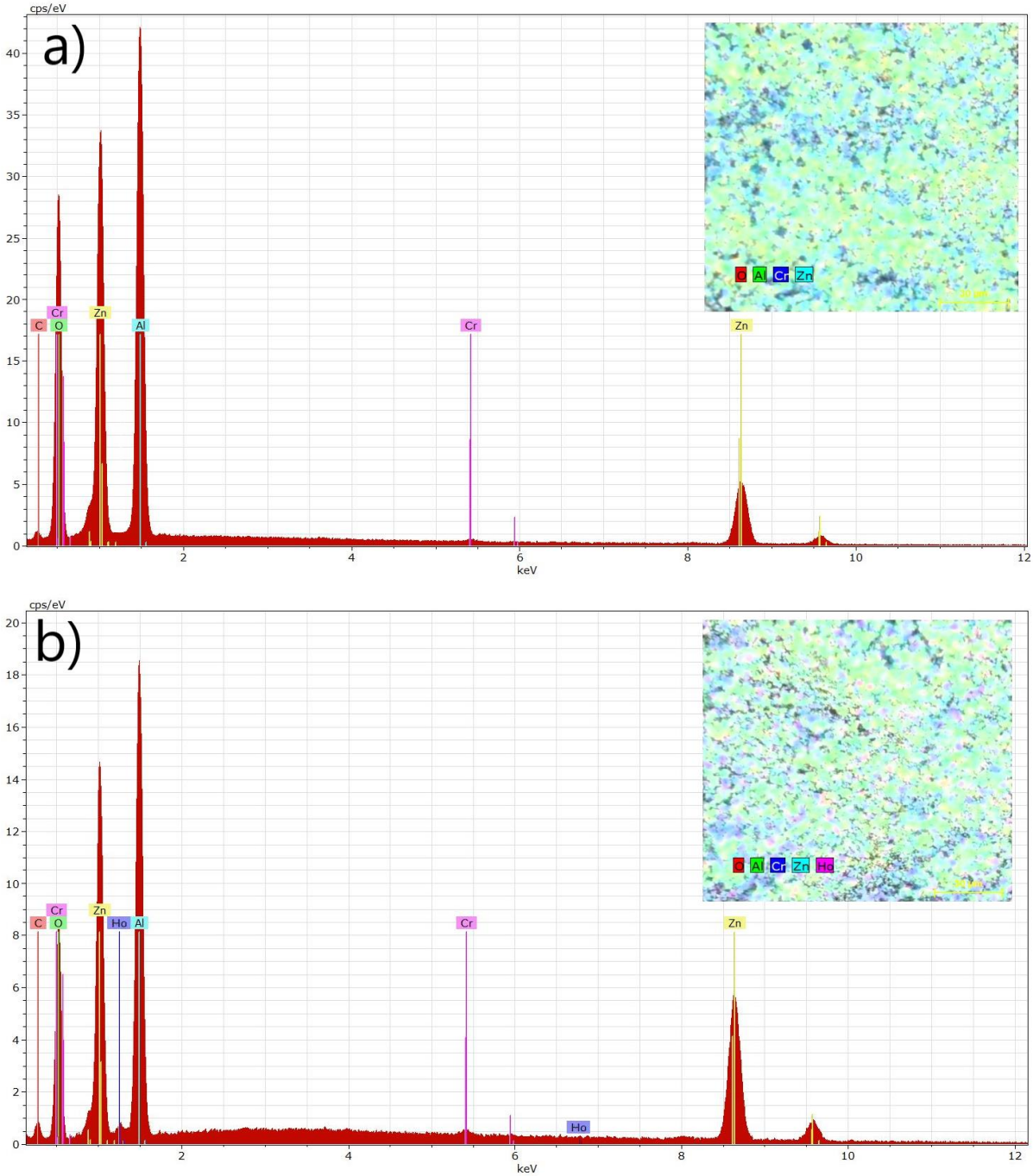

Figure 5. EDS spectrum of $ZnAl_{1.99-x}Ho_xCr_{0.01}O_4$ a) x=0 and b) 0.001 compounds

Table 2: EDX data of $ZnAl_{1.99-x}Ho_xCr_{0.01}O_4$ (with x=0, 0.001) spinels.

Element/ Symbol	**Series**	**Atomic (%)**	
		x=0	x=0.001
Aluminum/Al	K-series	50.22	48.80
Holmium/Ho	K-series	0	1.24
Chromium/Cr	K-series	12.56	13.03

Zinc/Zn	K-series	37.22	36.93

3.3 Raman and FTIR study

Zinc aluminate ($ZnAl_2O_4$) is a spinel-type compound that belongs to the cubic crystal system. In terms of Raman spectroscopy, the Raman-active vibrational modes depend on the symmetry of the crystal structure. For cubic crystals like spinels, there are several symmetry-allowed Raman modes associated with vibrational motions of the atoms in the crystal lattice. In the case of $ZnAl_2O_4$, which has a spinel crystal structure, the Raman-active modes are related to the vibrational motion of the oxygen, zinc, and aluminum atoms. Although the spinel unit cell has 56 atoms, only 14 atoms are needed to create the most basic primitive cell. Group theory, as initially introduced by White and DeAngelis [17], asserts that spinels near the center of the Brillouin zone possess a total of 42 normal modes, further categorized into 39 optical modes and 3 acoustic modes. These modes in terms of symmetry species are given by the following equation:

$$\mathbf{\Gamma(k=0) = E_g(R) \oplus A_{1g}(R) \oplus 3T_{2g}(R) \oplus T_{1g} \oplus 5T_{1u}(IR) \oplus 2T_{2u} \oplus 2A_{2u} \oplus 2E_u} \quad \mathbf{(2)}$$

where Raman and infrared-active are represented by the letters R and IR, respectively. There is one infrared active mode, T_{1u} (IR), and five Raman active modes (A_{1g} + E_g + $3T_{2g}$) [18,19]. In the case of spinel structures, five modes are observed. The Raman spectra of the $ZnAl_{1.99-x}Ho_xCr_{0.01}O_4$ (with x=0, 0.001) cubic spinel structure align closely with the literature [17,19] as illustrated in Figure 6. The frequencies of the observed phonons are detailed in Table 3. Prominent peaks with high intensity at 416 cm^{-1} and 658 cm^{-1} for the two samples are associated with the T_{2g} mode, involving the movement of oxygen atoms within AlO_6 octahedra, and the Eg mode, which entails the asymmetric bending movement of oxygen atoms in ZnO_4 tetrahedra. In $ZnAl_{1.99}Cr_{0.01}O_4$, other modes are observed with relatively low-intensity bands at 522 cm^{-1} and 200 cm^{-1}, which are assigned to the T_{2g} mode.

The infrared spectra for the two compounds in the 4000–400 cm^{-1} spectral range are shown in Figure 7. The sample exhibits prominent bands peaking at 667, 557, and 478 cm^{-1}, which are assigned to the Zn–O/Ho–O/Cr-O and Al–O stretching vibration modes of T_{1u} symmetry.

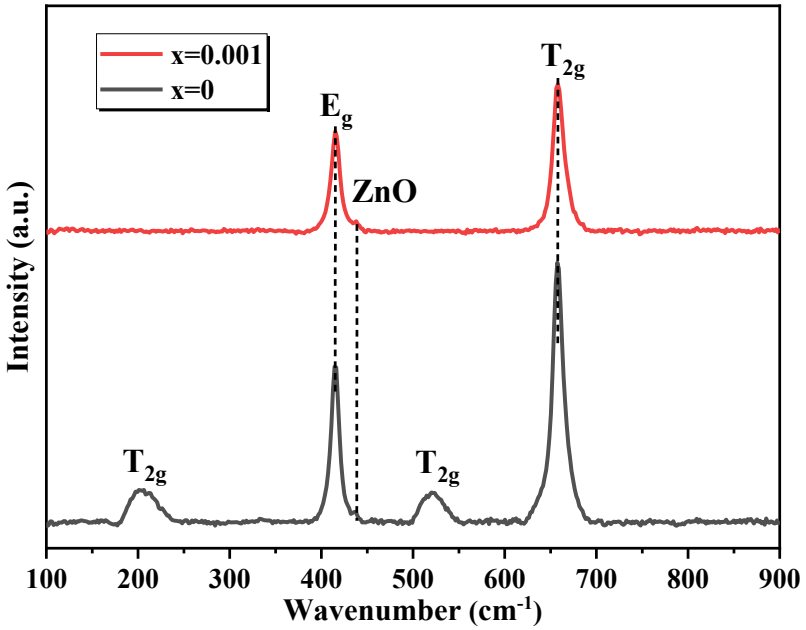

Figure 6. The Raman spectrum of $ZnAl_{1.99-x}Ho_xCr_{0.01}O_4$ (with x=0, 0.001) compounds

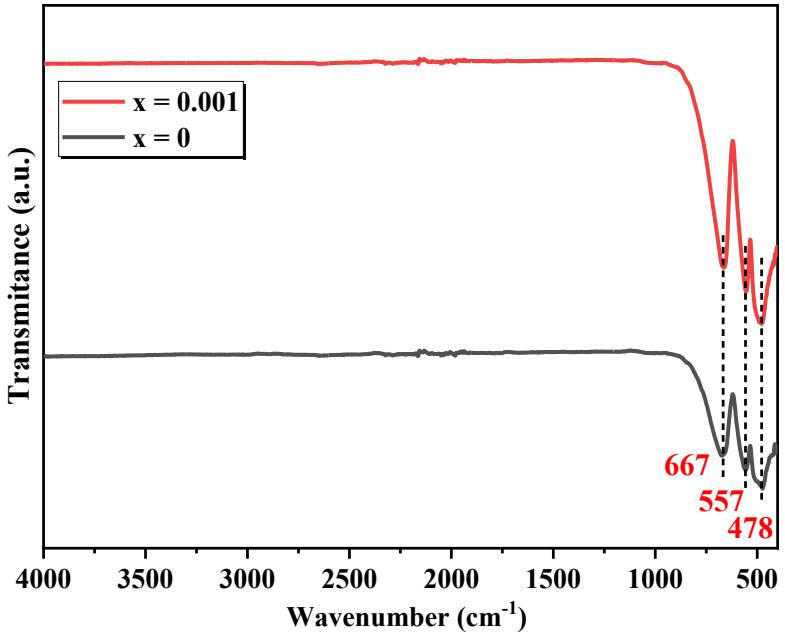

Figure 7. FTIR spectrum of $ZnAl_{1.99-x}Ho_xCr_{0.01}O_4$ (with x=0, 0.001) compounds

Table 3: Observed Infrared and Raman modes (in cm^{-1}) for $ZnAl_{1.99-x}Ho_xCr_{0.01}O_4$ (with x=0, 0.001) compounds.

	Raman modes (cm^{-1})		**Infrared modes (cm^{-1})**
	x = 0	**x = 0.001**	
T_{1u}	-	-	667

T_{2g}	658	658	-
T_{1u}	-	-	557
T_{2g}	522	-	-
T_{1u}	-	-	478
E_g	416	416	-
T_{2g}	200	-	-

3.4. Determination of the band-gap energy

The semiconductor $ZnAl_{1.99-x}Ho_xCr_{0.01}O_4$ (with x=0, 0.001) optical band gap E_g was calculated using Tauc's law, which is represented by the following equation [20]:

$$(\alpha h\nu)^{1/n} = A(h\nu - E_g) \quad (3)$$

where $h\nu$ is the energy of the incident photon in eV, E_g is the optical band gap energy, h is Planck constant (6.6×10^{-34}J.s), A is a band edge sharpness constant, α is the absorption coefficient and n is the exponent that fits the type of transition. The latter is equivalent to 2 or ½, depending on whether the gap is indirect or direct, respectively.

As shown in Figure 9, the plot of $(\alpha h\upsilon)^2$ as a function of the photon energy (hν) at high energy values (above 3.25 and 4 eV for the compound with x=0.001 and x=0, respectively) can be approached by a straight line. This straight line's extrapolation will intersect the (hν)-axis and yield the direct optical energy gap value E_g [21]. The estimated optical band gap for $ZnAl_{1.99}Cr_{0.01}O_4$ is equal to 3.70 eV and 3.12 eV for $ZnAl_{1.989}Ho_{0.001}Cr_{0.01}O_4$. We estimated an increase in the bandgap energy while estimating it for Ho-substituted spinel. This variation suggests that the bandgap energy decreases as particle size increases, as depicted in Figure 4. To validate the nature of optical band transition, we have restructured the relation (3) as follows:

$$Ln(\alpha h\nu) = n\,LnA + n\,Ln(h\nu - E_g) \quad (4)$$

The evaluation of Ln(αhν) versus Ln(hν - E_g) for the two samples is seen in Figure 10. The factor (n) is found when we trace the slope of the curve that we have gotten using equation (3). For the two compounds, n is close to ½ confirming the direct transition behavior as shown in Figure 10. The broad band gap of this spinel indicates its semiconductor nature, making it valuable for optoelectronic devices [22].

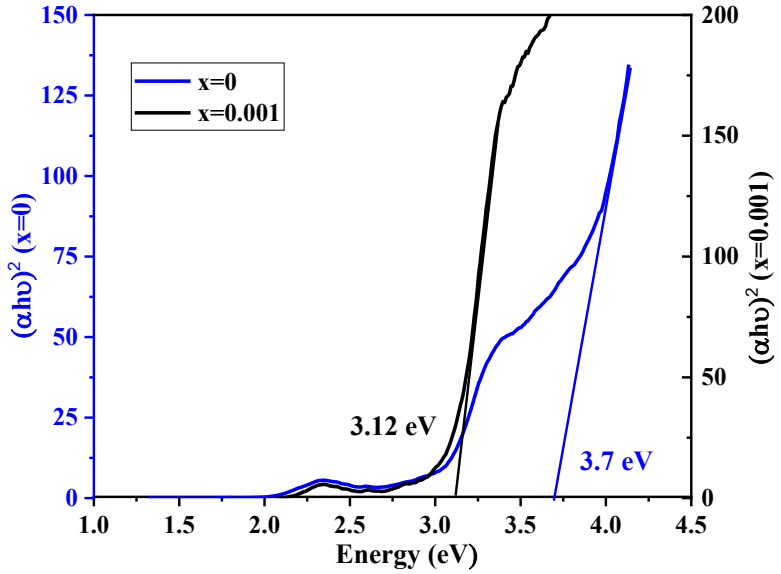

Figure 9. Evolution of $(\alpha h\upsilon)^2$ versus the energy hν of $ZnAl_{1.99-x}Ho_xCr_{0.01}O_4$ (with x=0, 0.001) compounds

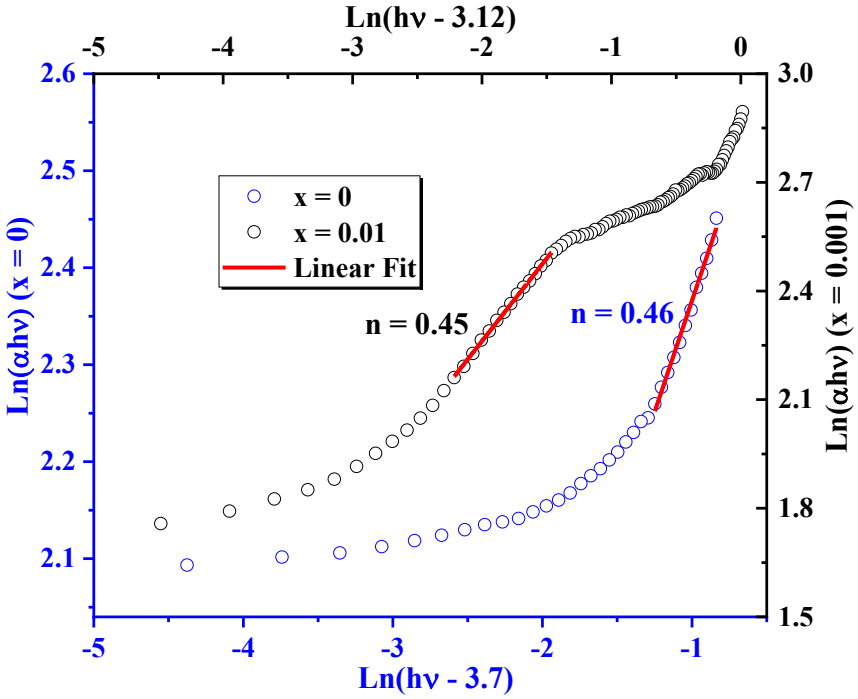

Figure 10. Evolution of Ln(αhν) against Ln(hν - E_g) of $ZnAl_{1.99-x}Ho_xCr_{0.01}O_4$ (with x=0, 0.001) compounds

3.5. Determination of Urbach energy E_u

The Urbach energy E_u is a parameter used to describe the exponential tail in the absorption edge of a semiconductor material. This tail is often observed in the absorption

spectrum of semiconductors and insulators, especially those with disordered structures or defects. Urbach energy quantifies the extent of disorder in a semiconductor material. It is the characteristic energy associated with the exponential decrease in absorption coefficient α near the absorption edge. The absorption coefficient α near the band edge is often described by the Urbach rule:

$$\alpha(E) = \alpha_0 \exp\left(\frac{E-E_g}{E_u}\right) \quad (5)$$

where α_0 is a pre-exponential factor, E_g is the bandgap energy, E is the photon energy, and E_u is the Urbach energy. A larger Urbach energy indicates a broader tail and, consequently, a higher degree of disorder in the material. It is often associated with the presence of defects, impurities, or structural disorders that create localized states within the bandgap. Urbach energy can be determined by analyzing the slope of the linear portion of the natural logarithm of the absorption coefficient versus photon energy in the Urbach tail region. Understanding the Urbach energy is crucial in characterizing the electronic properties and quality of semiconductor materials, particularly those used in optoelectronic devices such as solar cells and light-emitting diodes.

$$Ln(\alpha) = Ln(\alpha_0) + \frac{E - E_g}{E_u} \quad (6)$$

In Figure 9, the slope of the curve Ln(α) versus the energy E=hν yields the Urbach energy values of Eu = 325 meV for $ZnAl_{1.99}Cr_{0.01}O_4$ and Eu = 275 meV for $ZnAl_{1.989}Ho_{0.001}Cr_{0.01}O_4$, corresponding to 8.78% and 8.81% of the energy band-gap, respectively. This observation indicates a significant disorder in the compounds. There are three primary scientific explanations for this phenomenon; they are impurity-induced trap states [23], electron-phonon scattering [24,25], and crystal disorder [26].

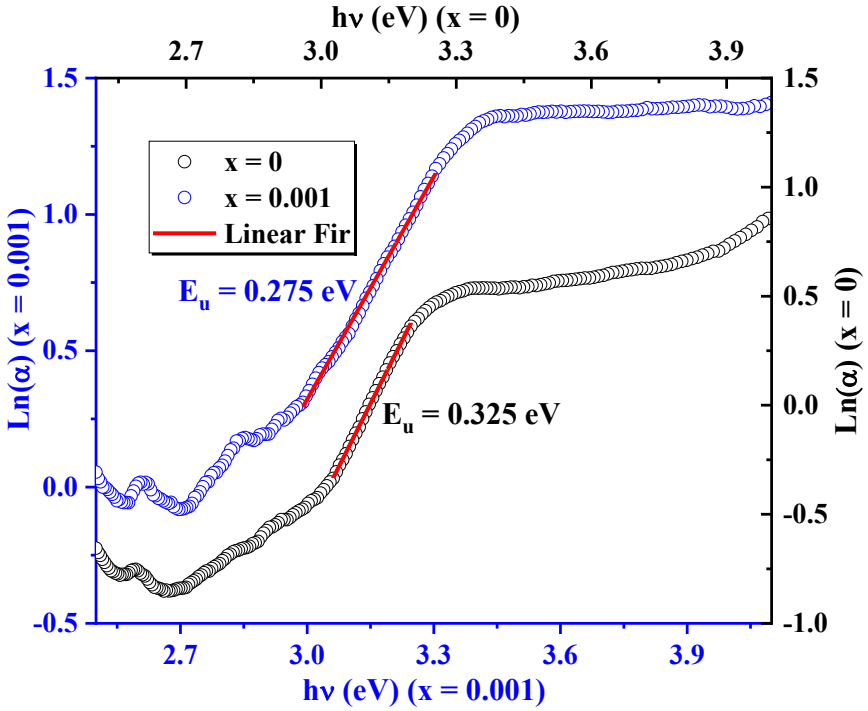

Figure 9. Variation of Ln(α) as a function of energy (eV) of $ZnAl_{1.99-x}Ho_xCr_{0.01}O_4$ (with x=0, 0.001) compounds

3-6 The 3d-3d transitions of $Cr^{3+}(3d^3)$ ions occupying an octahedral symmetry site in $ZnAl_{1.99-x}Ho_xCr_{0.01}O_4$ (with x=0, 0.001)

The study of 3d-3d transitions of metal ions highlights the complexity of their response to local environmental changes. These transitions, which involve the movement of electrons between 3d orbitals, exhibit remarkable sensitivity that is paramount in various scientific disciplines. The local environment, characterized by factors such as ligands, plays a central role in the formation of the electronic structure of metal ions. Therefore, spectroscopic analyses of these transitions often reveal broad absorption and emission bands [5,6]. The broadening of these bands constitutes a signature of the nuanced interactions between metal ions and their environment. This sensitivity has profound implications in fields such as coordination chemistry and materials science, where the design and manipulation of materials rely on a deep understanding of the electronic properties of metal-containing compounds. By exploiting the sensitivity of 3d-3d transitions, researchers can uncover valuable insights into the behavior of metal ions in various molecular contexts, facilitating the development of innovative materials and functional systems tailored to specific applications [5,6]. The room temperature optical absorption spectra in the UV/vis range between 300 and 700 nm of the two spinels $ZnAl_{1.99-x}Ho_xCr_{0.01}O_4$ (with x=0, 0.001) are shown in Figure 10. The peak in the UV region located at 367 nm (27248 cm^{-1}) is present for both spinels, it is attributed to arise from the band-to-band

transition and defects absorption within the host material [27]. The broad absorption band located at ~ 532 nm (green; 18797 cm^{-1}) for the two spinels is attributed to the d-d transitions of $Cr^{3+}(3d^3)$ ions occupying an O_h symmetry site.

Figure 11 illustrates the PLE spectrum, monitored at λ_{em} = 688 nm, of the $ZnAl_{1.99-x}Ho_xCr_{0.01}O_4$ (with x=0, 0.001) spinels measured at room temperature. This Figure shows two broad bands for each spinel:

- For spinel with x=0, the bands are located at 392 nm (25510 cm^{-1}) and 532 nm (18797 cm^{-1}); they are attributed respectively to $^4A_{2g}(^4F) \rightarrow {}^4T_{1g}(^4F)$ and $^4A_{2g}(^4F) \rightarrow {}^4T_{2g}(^4F)$ 3d-3d spin-allowed transitions.
- For spinel with x=0.001, the bands are located at 395 nm (25316 cm^{-1}) and 538 nm (18587 cm^{-1}); they are attributed respectively to $^4A_{2g}(^4F) \rightarrow {}^4T_{1g}(^4F)$ and $^4A_{2g}(^4F) \rightarrow {}^4T_{2g}(^4F)$ 3d-3d spin-allowed transitions.

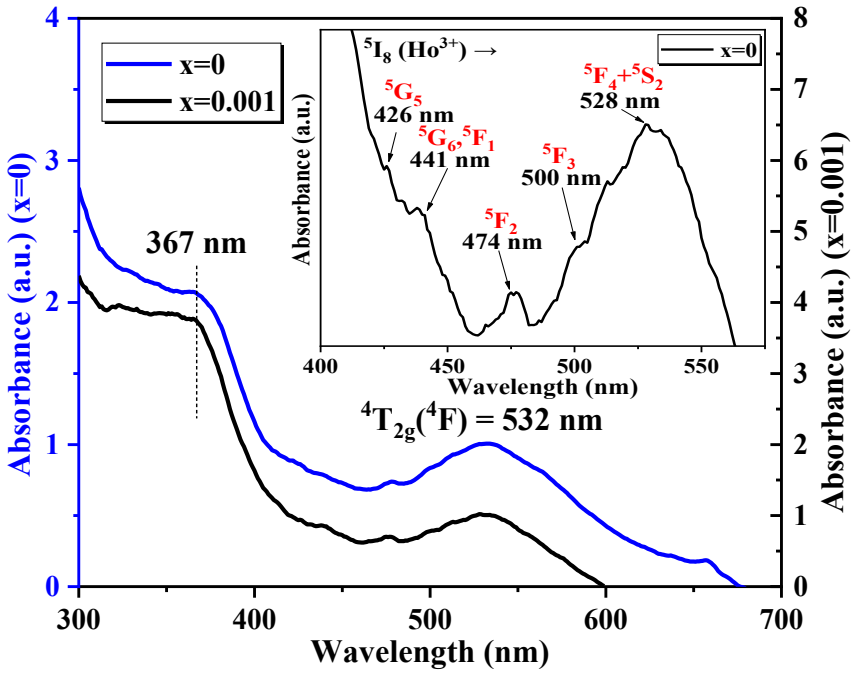

Figure 10. UV/vis optical absorption spectra of $ZnAl_{1.99-x}Ho_xCr_{0.01}O_4$ (with x=0, 0.001) recorded at room temperature in the 300-700 nm range.

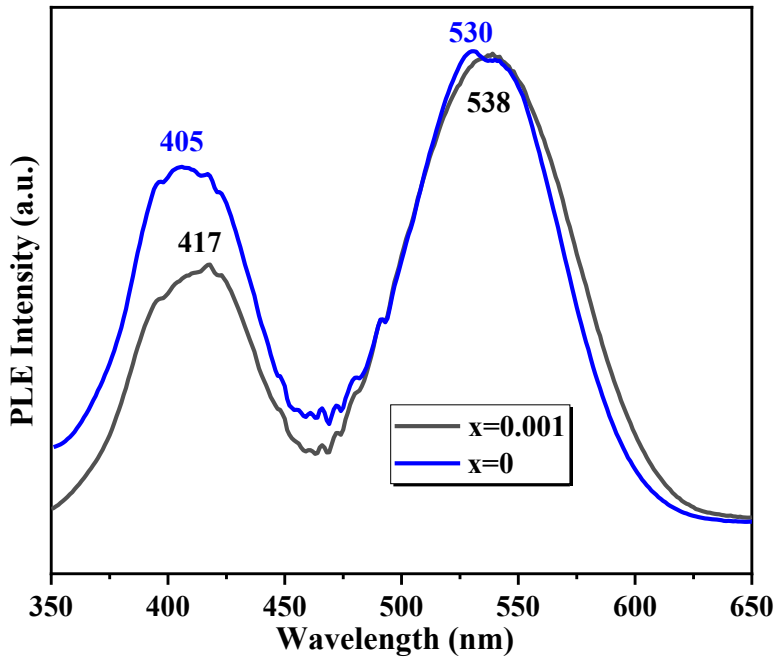

Figure 11. PLE spectra of $ZnAl_{1.99-x}Ho_xCr_{0.01}O_4$ (with x=0, 0.001) recorded at room temperature in the 300-700 nm range.

The investigation into the electronic structure of the $Cr^{3+}(3d^3)$ ion within the $ZnAl_{1.99-x}Ho_xCr_{0.01}O_4$ spinel, where x is either 0 or 0.001, was conducted using the following Hamiltonian [28-30]:

$$\mathbf{H = H_0 + H_{ee} + H_{Trees} + H_{CF} + H_{SO}} \qquad \mathbf{(7)}$$

This Hamiltonian serves as a mathematical representation of the system's energy and encompasses the Hamiltonian configuration $\mathbf{H_0}$ with the energy E_0 (120 times degenerated) of the free ion, the Hamiltonian $\mathbf{H_{ee}}$(B, C) (where B and C design the Racah parameters of electron-electron repulsions), the Trees correction Hamiltonian $\mathbf{H_{Trees}}(\alpha)$ (α being the Trees parameter), the crystal field Hamiltonian $\mathbf{H_{CF}}$ and the spin-orbit Hamiltonian $\mathbf{H_{SO}}(\zeta)$ (ζ being the spin-orbit coefficient) [31-34]. The Wybourne's notation gives the equation of the crystal field Hamiltonian $\mathbf{H_{CF}}$ for an octahedral symmetry [33]**:**

$$\mathbf{H_{CF}}(O_h) = -14 * Dq * \left[C_0^{(4)} - \frac{\sqrt{70}}{7}\left(C_{-3}^{(4)} - C_3^{(4)}\right)\right] \qquad \mathbf{(8)}$$

$\mathbf{H_{CF}}(O_h)$ is developed as a function of the Racah tensor operators $C_q^{(k)}$. The parameter Dq determines the crystal field strength [35-36]. In the LS-coupling scheme with the $\{|d^N LSM_L M_S\rangle\}$ basis function, the theoretical analysis was carried out using an intermediate crystal field [37-38]. The matrix elements of $C_q^{(k)}$ Racah tensor operators are calculated numerically. From the optical spectra, the Racah parameters B and C, and the crystal field

parameter Dq are determined. The Racah parameters B and C, the Trees correction constant α and the spin-orbit constant ζ can be estimated from the average reduction factor due to the covalency N and the parameters for the free Cr^{3+} ion (B_0 = 918 cm^{-1}, C_0 = 4,133 cm^{-1}, α_0 = 30 cm^{-1}, and ζ_0 =275 cm^{-1}) as:

$$\mathbf{B = N^4 B_0,\ C = N^4 C_0,\ \alpha = N^4 \alpha_0 \text{ and } \zeta = N^2 \zeta_0} \qquad \mathbf{(9)}$$

with:

$$\mathbf{N^2 = \frac{1}{2}\left(\sqrt{\frac{B}{B_0}} + \sqrt{\frac{C}{C_0}}\right)} \qquad \mathbf{(10)}$$

Using a code developed in our laboratory, which diagonalizes the 120×120 Hamiltonian matrices associated with the application of Equation 7, we obtain the theoretical energy levels as functions of the reduction factor N and crystal-field strength parameter Dq. These parameters were determined from the absorption and PLE spectra (Figures 10 and 11). From Dq and N parameters, the Racah B and C, the Trees correction α, and the spin-orbit coupling ζ parameters are determined using Equation 9 and are presented in Table 4. The calculated energy levels of $ZnAl_{1.99-x}Ho_xCr_{0.01}O_4$ (with x=0, 0.001) spinels are presented in Table 6. There is a good agreement between theoretical and experimental energy values. The Dq value for $ZnAl_{1.989}Ho_{0.001}Cr_{0.01}O_4$ is slightly lower than the value for $ZnAl_{1.99}Cr_{0.01}O_4$ (Table 4). This can be explained by the dependence of crystal field strength parameter Dq on the distance between Cr^{3+} ion and oxygen ligands.

The presence of Ho^{3+} lanthanide ions introduced a unique influence on the crystal field strength Dq. Lanthanides, such as Ho^{3+}, are characterized by their relatively large ionic radii. This size disparity can induce changes in the local coordination environment around neighboring transition metal ions, particularly chromium in this case. The crystal field strength Dq is influenced by the nature of the ligands and the geometry of the coordination environment. In the presence of larger lanthanide ions, the crystal field strength can be reduced due to several reasons:

- Increased Ionic Size: Lanthanide ions are generally larger than transition metal ions. The larger ionic size of Ho^{3+} can lead to a reduction in the effective crystal field strength experienced by the neighboring transition metal ion.
- Electronic Effect: Lanthanide ions have filled 4f orbitals, and their electronic structure can influence the electronic interactions in the crystal field, potentially leading to a reduction in Dq.

- Distortion of the Crystal Field: The introduction of a lanthanide ion can cause a distortion in the crystal field around the transition metal ion. This distortion may lead to a reduction in the energy difference between the d-orbitals.

The Racah (B and C) and the spin orbit ζ parameters are reduced compared to the free ion values (B_0, C_0 and ζ_0), this is due to covalency effects [37-38]. The values of the ratio $\beta_B = B/B_0$ and $\beta_C = C/C_0$ for the phosphor $ZnAl_{1.99-x}Ho_xCr_{0.01}O_4$ (with x=0, 0.001) have been evaluated (see Table 5). In free ions, the Racah parameters describe the energy of electron-electron repulsion and the energy difference between different configurations of the electronic states. In a complex, covalency between the metal and ligands leads to a mixing of metal d and ligand orbitals, creating a shared electron cloud. This covalent interaction reduces the electron-electron repulsion energy, leading to a decrease in *B* and *C* compared to their free ion values. The spin-orbit coupling parameter ζ determines the energy splitting between different spin states of an electron in a magnetic field created by its own motion. In covalent complexes, the metal-ligand interaction causes the electronic cloud to be distributed over both the metal and ligands. Covalency decreases the effective charge on the metal, reducing the strength of the spin-orbit interaction and resulting in a lower ζ compared to the free ion value. Covalency in transition metal complexes is a consequence of the sharing of electron density between the metal and ligands, leading to a more complex electronic structure than that of simple ionic models. The reduction in Racah parameters and spin-orbit coupling reflects the impact of these covalent interactions on the electronic properties of the metal ion in a complex.

Table 4: The Dq, B, C, α and ζ parameters (in cm^{-1}) for $ZnAl_{1.99-x}Ho_xCr_{0.01}O_4$ (with x=0, 0.001) and comparison with those of other spinels.

Materials	Dq	N^2	B	C	α	ζ
$ZnAl_{1.99}Cr_{0.01}O_4$[This work]	1880	0.841	649	2921	21.206	231.206
$ZnAl_{1.989}Ho_{0.001}Cr_{0.01}O_4$[This work]	1858	0.844	654	2943	21.367	232.085
$ZnAl_{1.99}Cr_{0.05}O_4$[ref precedent]	1886	0.848	660	2970	21.563	233.14
$MgAl_2O_4$: Cr^{3+} [39]	1825	/	700	3200	/	250
$BaAl_2O_4$ Cr^{3+} [39]	1811	/	533	/	/	/

Table 5: The ratio $\beta_B = B/B_0$ and $\beta_C = C/C_0$ for the phosphor $ZnAl_{1.99-x}Ho_xCr_{0.01}O_4$ (with x=0, 0.001).

Materials	Dq/B	C/B	B/B0	C/C0

$ZnAl_{1.99}Cr_{0.01}O_4$ [This work]	2.90	4.50	0.71	707
$ZnAl_{1.989}Ho_{0.001}Cr_{0.01}O_4$ [This work]	2.84	4.50	0.71	712
$ZnAl_{1.99}Cr_{0.05}O_4$ [39]	2.86	4.50	0.72	719

Table 6: Calculated energy levels (in cm^{-1}) for the $ZnAl_{1.99-x}Ho_xCr_{0.01}O_4$ (with x=0, 0.001) spinels.

O_h	E_i^{obs}	$E_i^{cal}(O_h)$	$E_i^{cal}(O_h)$ with Spin-orbit interaction		E_i^{obs}	$E_i^{cal}(O_h)$	$E_i^{cal}(O_h)$ with Spin-orbit interaction	
$^4A_{2g}(^4F)$	0	0	G	0	0	0	G	0
$^2E_g(^2G)$		13626	G	13761		13720	G	13854
$^2T_{1g}(^2G)$		14180	G	14304		14281	G	14405
			E_1	14362			E_1	14465
$^4T_{2g}(^4F)$	18797	18800	E_1	18705		18580	E_1	18485
			G	18758			G	18539
			E_2	18870			E_2	18651
			G	18872			G	18653
$^2T_{2g}(^2G)$		20819	G	20891		20925	G	20996
			E_2	20999			E_2	21105
$^4T_{1g}(^4F)$	25510	25508	G	25396	25316	25313	G	25200
			E_2	25400			E_2	25205
			E_1	25410			E_1	25218
			G	25414			G	25221
$^2A_{1g}(^2G)$		30159	E_1	30342		30025	E_1	30210
$^2T_{1g}(^2P)$		32275	E_1	32474		32151	E_1	32352
			G	32521			G	32398
$^2T_{1g}(^2H)$		32599	E_1	32692		32484	E_1	32577
			G	32867			G	32753
$^2E_g(^2H)$		34190	G	34325		34087	G	34222
$^2T_{1g}(^2H)$		37286	E_1	37348		37189	E_1	37251
			G	37388			G	37290
$^4T_{1g}(^4P)$		40627	E_2	40475		40237	E_2	40090
			G	40495			G	40107
				40595				40204
			E_1	40636			E_1	40242
$^2T_{2g}(^2H)$		41741	G	41652		41704	G	41611
			E_2	41652			E_2	41711
$^2A_{2g}(^2F)$		43139	E_2	43149		43105	E_2	43115
$^2T_{2g}(^2D_a)$		51005	E_2	51255		50668	E_2	50921
			G	51366			G	51032
$^2E_g(^2D_a)$		51920	G	51911		51874	G	51867
$^2T_{2g}(^2F)$		52357	E_2	52400		52046	E_2	52087
			G	52506			G	52196
$^2T_{1g}(^2F)$		57240	E_1	57136		56972	E_1	56868

			G	57262			G	56993
$^2T_{2g}(^2D_b)$		71080	G	70948		70929	G	70797
			E_2	71146			E_2	70994
$^2E_g(^2D_b)$		75397	G	75462		74969	G	75031

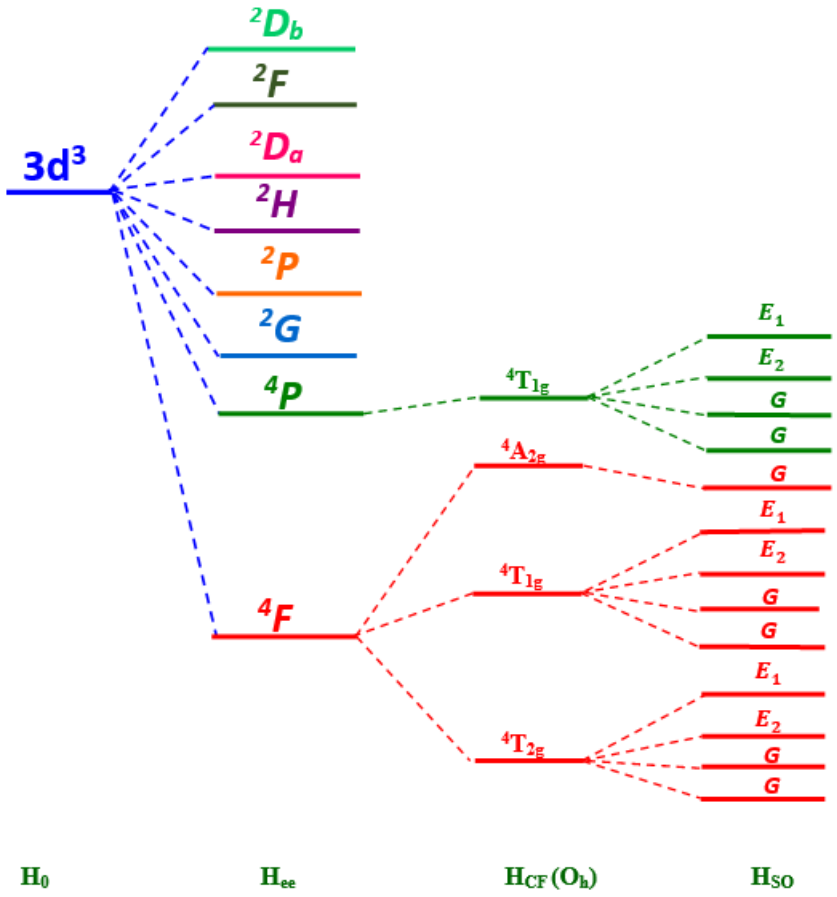

Figure 12. Diagram of the first electronic states for the Cr^{3+} $3d^3$ configuration in the $ZnAl_{1.99}Cr_{0.01}O_4$ sample.

Figure 12 illustrates the initial energy levels of the Cr^{3+} ion with $3d^3$ electronic configuration under the influence of a crystal field of O_h symmetry and spin-orbit coupling.

The bonding nature is evaluated by the following expression [40]:

$$\mathbf{h = [\frac{B_0 - B}{B_0 k}]} \quad \textbf{(11)}$$

For the Cr^{3+} ion, k is equal to 0.21 [41]. The pronouncedly high value of h (1.3954 for $ZnAl_{1.99}Cr_{0.01}O_4$ and 1.3694 for $ZnAl_{1.989}Ho_{0.001}Cr_{0.01}O_4$) in the context of the electronic structure analysis signifies a noteworthy degree of delocalization of d-d electrons within the Cr^{3+} ion. This observation strongly suggests that the prevailing bonding between Cr^{3+} and its ligands leans predominantly towards an ionic character. In the realm of coordination chemistry, a heightened h value indicates a substantial dispersion of electron density, pointing to the diminished localization of electrons specifically within the d orbitals of the chromium ion. This manifestation aligns with the conceptual framework of ionic bonding, wherein electrons undergo transfer between the metal ion (Cr^{3+}) and its ligands, resulting in a more diffuse

distribution of electron density. Such insights into the bonding nature are pivotal, offering a nuanced understanding of the electronic interactions at play within the system and contributing to a comprehensive comprehension of the compound's chemical and physical properties.

Figure 13 illustrates the Tanabe-Sugano diagram for Cr^{3+} ion in the O_h octahedral symmetry site (the ratio C/B is equal to 4.50). This diagram is a fundamental tool for comprehending the electronic transitions and energy levels of transition metal ions within octahedral or tetrahedral coordination environments. It is crucial for understanding the electronic structure changes of transition metal ions as the ligand field strength varies. The two vertical lines for Dq/B shown in Figure 13 represent the calculated energies values found for Cr^{3+} in the $ZnAl_{1.99-x}Ho_xCr_{0.01}O_4$ (with x=0, 0.001) phosphor.

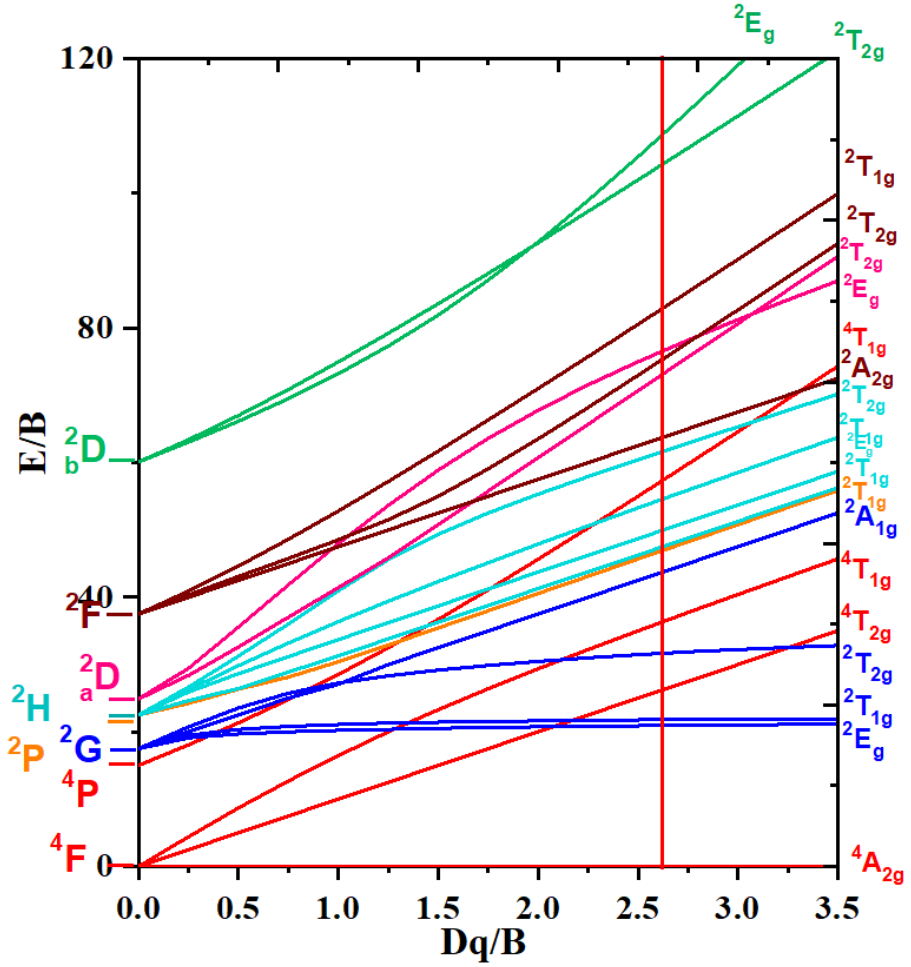

Figure 13. Tanabe–Sugano diagram for octahedrally coordinated Cr^{3+} ion with C/B = 4.50. The vertical lines represent the case of Cr^{3+} in the $ZnAl_{1.99-x}Ho_xCr_{0.01}O_4$ (with x=0, 0.001) spinel.

3.7 The 4f-4f transition of Ho^{3+} ions in $ZnAl_{1.989}Ho_{0.001}Cr_{0.01}O_4$spinel

On the absorption spectrum in Figure 10 of the $ZnAl_{1.989}Ho_{0.001}Cr_{0.01}O_4$ spinel and in addition to the 3d-3d transitions appear several peaks at 426, 441, 474, 500 and 528 nm. These peaks are assigned to the 4f-4f transitions of Ho^{3+} ion with $4f^{10}$ electronic configuration [42]. On the contrary to metal transition ions, the 4f electrons optically active for the lanthanides are screened by the $4s^24p^6$ layers. Then these electrons weakly feel the effects of the outside and it is a weak crystal field. The optical spectra of rare earth ions are characterized by narrow 4f-4f transitions. Furthermore, the positions of these transitions are almost identical to those of the free ion and do not depend on the host matrix in which they are incorporated. For this reason, the assignment of the 4f-4f transitions of Ho^{3+} is based on the comparison with energy level scheme of Ho^{3+} in the $HoCrO_3$ perovskite compound [42]. Table 7 presents the Ho^{3+} transitions from the ground state $^5I_8$ (Ho^{3+}) to different excited states. The presence of these transitions indicates that Ho^{3+} ions have been well incorporated into the normal spinel $ZnAl_{1.989}Ho_{0.001}Cr_{0.01}O_4$). From Figure 10, we remark that the absorption bands $^5I_8(Ho^{3+}) \rightarrow {}^5G_5(Ho^{3+})$ (426 nm),$^5I_8(Ho^{3+}) \rightarrow {}^5G_6(Ho^{3+})$ $^5F_1(Ho^{3+})$ (441 nm),$^5I_8(Ho^{3+}) \rightarrow {}^5F_2(Ho^{3+})$ (474 nm), $^5I_8(Ho^{3+}) \rightarrow {}^5F_3(Ho^{3+})$ (500 nm) and $^5I_8(Ho^{3+}) \rightarrow {}^5F_3(Ho^{3+})+{}^5S_2(Ho^{3+})$ (528nm) are relatively intense and sharp.

Table 7: 4f-4f (Ho^{3+}) absorption energy (in nm) for $ZnAl_{1.989}Ho_{0.001}Cr_{0.01}O_4$ spinel.

Peaks	Transitions
426	$^5I_8(Ho^{3+}) \rightarrow {}^5G_5(Ho^{3+})$
441	$^5I_8(Ho^{3+}) \rightarrow {}^5F_1, {}^5G_6(Ho^{3+})$
474	$^5I_8(Ho^{3+}) \rightarrow {}^5F_2(Ho^{3+})$
500	$^5I_8(Ho^{3+}) \rightarrow {}^5F_3(Ho^{3+})$
528	$^5I_8(Ho^{3+}) \rightarrow {}^5F_4(Ho^{3+}) + {}^5S_2(Ho^{3+})$

3.10 Electronic paramagnetic resonance (EPR)

Electron Paramagnetic Resonance (EPR), also known as Electron Spin Resonance (ESR), is a spectroscopic technique used to study materials with unpaired electrons, such as free radicals or paramagnetic ions. $ZnAl_2O_4$, or zinc aluminate, is a spinel-type compound that can exhibit interesting magnetic properties. Traps in the context of semiconductors and materials science generally refer to localized energy states within the bandgap that can capture and release charge carriers (electrons or holes). These traps play a crucial role in the electronic

properties of materials. The nature of traps in $ZnAl_2O_4$ (zinc aluminate) can vary, and they may be associated with different defects or impurities in the crystal lattice. Here are some possible types of traps that could be present in $ZnAl_2O_4$:

1- Interstitial Metal ions: Traps can be created by the presence of interstitial metal ions (e.g., Zn^{2+} or Al^{3+}) that do not occupy regular lattice sites.
2- Substructional impurities: If foreign ions replace the Zn^{2+} or Al^{3+} ions in the crystal lattice, they can introduce energy levels within the bandgap, acting as traps for charge carriers.
3- Vacancies, where atoms are missing from their regular lattice positions, can create localized states in the bandgap, acting as traps for charge carriers.
4- Surface states: Traps may also be associated with surface defects or states at the interfaces of the material. Surface traps can influence the charge transport properties, especially in nanoscale materials.
5- Charge compensated defects: Complex defects where charge compensation is not perfect can create localized states acting as traps.
6- Oxygen vacancies: In oxides like $ZnAl_2O_4$, oxygen vacancies can create traps for charge carriers.

The presence and characteristics of traps in $ZnAl_2O_4$ can depend on the specific synthesis method, processing conditions, and any intentional or unintentional doping or impurity incorporation. Experimental techniques, such as deep-level transient spectroscopy (DLTS) or thermally stimulated current (TSC) measurements, can be employed to study and characterize traps in a material like $ZnAl_2O_4$. Additionally, theoretical calculations and modeling may provide insights into the nature of these traps. Figure 14 depicts the EPR spectrum of the $ZnAl_{1.99-x}Ho_xCr_{0.01}O_4$ (with x=0, 0.001) powder phosphor samples at room temperature. The spectrum shows a prominent resonance signal centered at g = 3.84 and a weaker signal at g = 1.99. A recent study by Giada Lorenzi et al. [43] on the EPR spectrum of Cr-bearing gahnite ($ZnAl_2O_4$) pigment at X and W band frequencies revealed two resonance signals at g values of 3.87 and 2.05. Notably, our study also observes similar resonance signals, with a higher intensity at g = 3.87 compared to g = 2.05. The increasing signal strength at approximately g = 3.84 suggests the presence of additional emission centers in the spinel lattices [44]. As expected, no resonance signals corresponding to Ho^{3+} ions were observed at room temperature [45].

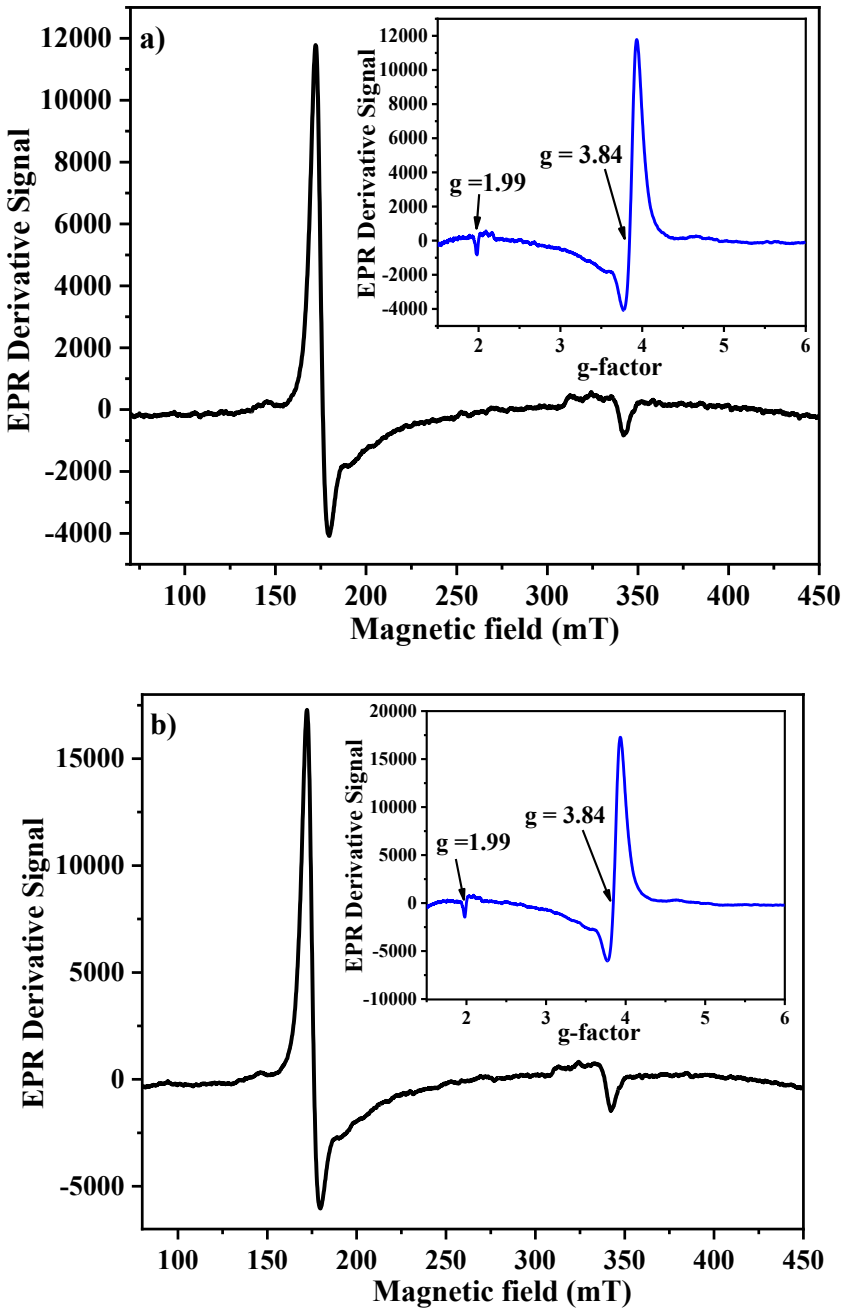

Figure 14. EPR spectrum and g-factor of $ZnAl_{1.99-x}Ho_xCr_{0.01}O_4$ with a) x=0 and b) 0.001 spinels at room temperature

4. Conclusion

In summary, our investigation systematically delved into the synthesis and characterization of $ZnAl_{1.99-x}Ho_xCr_{0.01}O_4$ spinels, where x=0 and 0.001, focusing on the optoelectronic properties resulting from Ho^{3+} and Cr^{3+} co-doping. Through XRD analysis, SEM imaging,

Energy Dispersive X-ray analysis, as well as Raman, infrared, and EPR measurements, we confirmed the cubic spinel structure, assessed morphology and chemical homogeneity, and gained valuable insights into the materials. Our findings regarding the optical behavior, as revealed by UV/vis. absorption spectra and Tauc's law, underscored the direct transition characteristics, with the presence of Cr^{3+} and Ho^{3+} ions contributing to increased disorder and defect concentration. EPR measurements provided further insights into different types of traps, enriching our understanding of the electronic structure. Notably, room temperature absorption spectra displayed distinct peaks corresponding to transitions of Cr^{3+} and Ho^{3+} ions, suggesting promising applications of these compounds in optoelectronic devices. Overall, this study not only advances our understanding of spinel structures but also highlights the potential practical implications of the synthesized compounds in optoelectronic technologies.

Statements & Declarations:

- Ethical Approval: Disclosure of potential conflicts of interest
- Consent to Participate: All authors agreed to participate in this study.
- Consent to Publish: All authors have agreed to publish this work in the **Dalton Transactions** Journal.
- Authors Contributions: All authors contributed to the conception and design of the study. Material preparation, data collection, and analysis were performed by **I. Elhamdi, H. Souissi, S. Kammoun, E. Dhahri, J. Pina, B. F. O. Costa and E. López-Lago**. All authors commented on the previous versions of the manuscript. All the authors have read and approved the final manuscript.
- Funding: No funds, grants, or other support was received during the preparation of this work.
- Competing Interests: The authors have no relevant financial or non-financial interests to disclose.
- Availability of data and materials: Data sharing is not applicable to this article as no datasets were generated or analyzed during the current study.

References

[1] B. Qiao, Z. L. Tang, Z.T. Zhang, L. Chen; Photoluminescent and electroluminescent characteristics of $ZnGa_2O_4$:Cr^{3+} red phosphor; Acta Phys. Chim. Sin. 22(10) (2006) 1291–1295.

[2] C. R. Garcia, J. Oliva, L.A. Diaz-Torres, E. Montes, G. Hirata, J. Bernal Alvarado, C. Gomez-Solis; Controlling the white phosphorescence $ZnGa_2O_4$ phosphors by surface defects, Ceram. Int. 45 (2019) 4972–497.

[3] W.A.I. Tabaza, H.C. Swart, R.E. Kroon, Luminescence of Ce doped $MgAl_2O_4$ prepared by the combustion method, Physica B 439 (2014) 109–114.

[4] V. Singh, R.P.S. Chakradhar, J.L. Raoc, D.K. Kim, Characterization, EPR and luminescence studies of $ZnAl_2O_4$: Mn phosphors, J. Lumin.128 (2008) 394–402.

[5] I. Elhamdi, H. Souissi, S. Kammoun, E. Dhahri, A.L.B. Brito, R. Fausto, B.F.O. Costa; Experimental determination and modeling of structural, vibrational and optical properties of the $ZnAl_{2-x}Cr_xO_4$ (x = 0 and 0.05) spinels, J. Lumin; 263 (2023) 119968.

[6] I. Elhamdi, F. Mselmi, H. Souissi, S. Kammoun, E. Dhahri, P. Sanguino and B. F. O. Costa; Summerfield scaling model and electrical conductivity study for understanding transport mechanisms of a Cr^{3+} substituted $ZnAl_2O_4$ ceramic; RSC Adv.; 13 (2023) 3377-3393.

[7] M. G. Brik, J. Papan, D. J. Jovanović, M. D. Dramićanin; Luminescence of Cr^{3+} ions in $ZnAl_2O_4$ and $MgAl_2O_4$ spinels: correlation between experimental spectroscopic studies and crystal field calculations; J. Lumin 177 (2016) 145-151.

[8] M. T. Tran, D. Q. Trung, N. Tu, D. D. Anha, L. T. H. Thu, N. V. Du, N. V. Quang, N. T. Huyen, N. D. T. Kien, D. X. Viet, N. D. Hung, P. T. Huy; Single-phase far-red-emitting $ZnAl_2O_4$:Cr^{3+} phosphor for application in plant growth LEDs, J. Alloys Compd. 884 (2021) 161077.

[9] S. V. Motloung, F. B. Dejene, H. C. Swart, O. M. Ntwaeaborwa; Effects of Cr^{3+} mol% on the structure and optical properties of the $ZnAl_2O_4$:Cr^{3+} nanocrystals synthesized using sol–gel process, Ceram. Itnl. B 41 (2015) 6776–6783.

[10] S. P. Huang, Z. Q. Wei, X. J. Wu, J. W. Shi; Optical properties of Cr doped $ZnAl_2O_4$ nanoparticles with Spinel structure synthesized by hydrothermal method, Mater. Res. Express 7 (2020) 015025.

[11] I. Elhamdi, F. Mselmi, S. Kammoun, E. Dhahri, A. J. Carvalho, P. Tavares and B. F. O. Costa; A far-red-emitting $ZnAl_{1.95}Cr_{0.05}O_4$ phosphor for plant growth LED applications; Dalton Trans.; 52 (2023) 9301-9314.

[12] N. G. Kostova, Al. Eliyas, M. Fabián, M. Achimovičová and P. Baláž; Photocatalytic Properties of Mechanochemically Synthesized Nanocrystalline $ZnAl_2O_4$ and CdSe; Acta Phys. Pol. A; 126 (2014) 967-970.

[13] S. V. Motloung, P. Kumari, L. F. Koao, T. E. Motaung, T. T. Hlatshwayo and M. J. Mochane; Effects of annealing time on the structure and optical properties of $ZnAl_2O_4$/ZnO prepared via citrate sol-gel process; Mater. Today Commun.; 14 (2018) 294-30.

[14] M. Kumar, V. Natarajan and S. V. Godbole; Synthesis, characterization, photoluminescence and thermally stimulated luminescence investigations of orange red-emitting Sm^{3+}-doped $ZnAl_2O_4$ phosphor, Bull. Mater. Sci., 37 (2014) 1205–1214.

[15] V. Singh, G. Sivaramaiah, J. L. Rao, S J Dhoble, And S H Kim; Electron Paramagnetic Resonance and Photoluminescence Studies of Ultraviolet-Emitting $ZnAl_2O_4$:Gd^{3+} Phosphors, J. of Electronic Materials; 139 (2015) 1-6.

[16] I. Elhamdi, H. Souissi, O. Taktak, J. Elghoul, S. Kammoun, E. Dhahri and B. F. O. Costa; Experimental and modeling study of ZnO:Ni nanoparticles for near-infrared light emitting diodes; RSC Adv.; 12 (2020) 13074-13086.

[17] W. B. White and B. A. D. Angelis; Interpretation of the vibrational spectra of spinels; Spectrochimica Acta Part A; 23 (1967) 985–995.

[18] A. Kumar, M. A. Dar, P. Sharma and D. Varshney; Structural And Raman Scattering Study Of Ni-doped $CoFe_2O_4$ AIP Conference Proceedings (2014) 1591, 1148.

[19] C. M. Fang, C. K. Loong, G. A. de Wijs, and G. de With; Phonon spectrum of $ZnAl_2O_4$ spinel from inelastic neutron scattering and first-principles calculations; Physical Review B; 66 (2002) 144301.

[20] G. D. Cody, T. Tiedje, B. Abeles, B. Brooks, Y. Goldstein, Disorder and the Optical Absorption Edge of Hydrogenated Amorphous Silicon, Phys. Rev. Lett., 47 (1981) 1480-1483.

[21] G. S. Shahane, B. M. More, C. B. Rotti, L. P. Deshmukh, Mater. Chem. Phys., 47(1997) 263.

[22] S. Kalyanaraman, P. M. Shajinshinu and S. V. Jayalakshmi; Determination of optical constants and polarizability studies on ferroic Tetramethylammonium Tetracholorozincatecrystal, Physica B; 482 (2016) 38-42.

[23] J. Pospisil, O. Zmeskal, S. Nespurek, J. Krajcovic, M. Weiter and A. Kovalenko; Density of bulk trap states of hybrid lead halide perovskite single crystals: temperature modulated space-charge-limited-currents; Sci. Rep. 9 (2019) 3332.

[24] R. C. Ram; Analysis of the Urbach tails in absorption spectra of undoped ZnO thin films J. Appl. Phys. 113 (2013) 153508.

[25] C. H. Grein and S. John; Temperature dependence of the Urbach optical absorption edge: A theory of multiple phonon absorption and emission sidebands Phys. Rev. B 39 (1989) 1140-1151.

[26] G. D. Cody; Urbach edge of crystalline and amorphous silicon: a personal review J. Non-Cryst. Solids, 141(1992) 3-15.

[27] S. V. Motloung, S. J. Motloung, H. C. Swart, T. T. Hlatshwayo; The effect of annealing time on the structural and optical properties of $ZnAl_2O_4$:0.01% Cr^{3+} nanophosphor prepared via sol-gel method; J. Electron. Mater.; 47 (2018) 521–529.

[28] O. Taktak, H. Souissi, S. Kammoun, Optical absorption properties of ZnF_2-RO-TeO_2 (R = Pb, Cd and Zn) glasses doped with chromium (III): Neuhauser model and crystal field study, Opt. Mater., 113 (2021) Art. 110682.

[29] H. Souissi, O. Taktak, S. Kammoun, Crystal field study of chromium (III) ions doped antimony phosphate glass: Fano's antiresonnance and Neuhauser models, Ind. J. Phys., 92 (2018) 1153–1160.

[30] O. Maalej, O. Taktak, B. Boulard, S. Kammoun, Study with analytical equations of absorption spectra containing interference dips in fluoride glasses doped with Cr^{3+}, J. Phys. Chem. B, 120 (2016) 7538–7545.

[31] H. Souissi, O. Taktak, O. Maalej, S. Kammoun, Electronic structure and Fano's antiresonance study of Cr^{3+} doped BIGaZYTZr fluoride glass, J. New Technol. Mater., 6 (2016) 34–41.

[32] O. Taktak, H. Souissi, O. Maalej, B. Boulard, S. Kammoun, Fano's antiresonance and crystal-field study of Cr^{3+} in metaphosphate glasses, J. Lumin., 180 (2016) 183–189.

[33] O. Taktak, H. Souissi, S. Kammoun, Electronic structure and Fano antiresonance of chromium Cr(III) ions in alkali silicate glasses, J. Lumin., 161 (2015) 368–373.

[34] H. Souissi, S. Kammoun, Theoretical study of the electronic structure of a tetragonal chromium(III) complex, J. Lumin., 131 (2011) 2515–2520.

[35] S. Kammoun, J. El Ghoul, Structural and optical investigation of Co-doped ZnO nanoparticles for nanooptoelectronic devices, J. Mater. Sci.: Materials in Electronics, 32 (2021) 7215–7225.

[36] F. Mselmi, O. Taktak, H. Souissi, S. Kammoun, Correlation between experimental spectroscopic study and crystal-field calculations of Co^{2+} ions in α-$ZnAl_2S_4$ spinel J. Lumin., 206 (2019) 319–325.

[37] F. Mselmi, A. Neffati, S. Kammoun, Theoretical investigation of the cathode-luminescence spectra of Co-doped ZnO nanowires, J. Lumin., 198 (2018) 124–131.

[38] A. Neffati, H. Souissi, S. Kammoun, Electronic structure of co-doped ZnO nanorods J. Appl. Phys., 112 (2012) Art. 083112.

[39] S. G. Menon, D. N. Hebbar, S. D. Kulkarni, K. S. Choudhari, C. Santhosh, Facile synthesis and luminescence studies of nanocrystalline red emitting Cr:$ZnAl_2O_4$ phosphor, Mater. Res. Bull., 86 (2017) 63–71.

[40] W. Seeber, D. Ehrt, D. Eberdorff-Heidepriem, Spectroscopic and laser properties of Ce^{3+}, Cr^{3+}, Nd^{3+} co-doped fluoride phosphate and phosphate glasses, J. Non-Cryst. Sol., 171 (1994) 94–104.

[41] C. K. Jorgensen, H. Hartmann, Absorption spectra and chemical bonding in complexes, Pergamon Press, Oxford (UK), 1963, pp. 113.

[42] R. Mguedla, A. Ben Jazia Kharrat, S. Kammoun, K. Khirouni, W. Boujelben; Optical studies of multiferroic HoCrO3 perovskite compound for optoelectronic device applications; Optical Materials 119 (2021) 111311.

[43] G. Lorenzi, G. Baldi, F. Di Benedetto, V. Faso, L. A. Pardi, and M. Romanelli; HF2EPR investigation of a Cr-bearing gahnite pigment; Journal of the European Ceramic Society; 26 (200) 125–129.

[44] D. Zhang, Q. Guo, Y. Ren, C. Wang, Q. Shi, Q. Wang, X. Xiao, W. Wang and Q. Fan; Influence of inversion defects and Cr–Cr pairs on the photoluminescent performance of $ZnAl_2O_4$ crystals; Journal of Sol-Gel Science and Technology; 85 (2018)121–131.

[45] M. Popa, G.Schmerber, D. Toloman, M. S. Gabor, A. Mesaros, T. Petrişor; Magnetic and Electrical Properties of Undoped and Holmium Doped ZnO Thin Films Grown by Sol-Gel Method; Advanced Engineering Forum; 8-9 (2013) 301-308.